Pattern recognition in multi-synaptic photonic spiking neural networks based on a DFB-SA chip

Yanan Han, Shuiying Xiang, Ziwei Song, Shuang Gao, Xingxing Guo, Yahui Zhang, Yuechun Shi, Xiangfei Chen and Yue Hao

---

Related articles

Photonic synapses with ultralow energy consumption for artificial visual perception and brain storage
Caihong Li, Wen Du, Yixuan Huang, Jihua Zou, Lingzhi Luo, Song Sun, Alexander O. Govorov, Jiang Wu, Hongxing Xu, Zhiming Wang
Opto-Electronic Advances   2022 **5**, 210069   doi: 10.29026/oea.2022.210069

Direct field-to-pattern monolithic design of holographic metasurface via residual encoder-decoder convolutional neural network
Ruichao Zhu, Jiafu Wang, Tianshuo Qiu, Dingkang Yang, Bo Feng, Zuntian Chu, Tonghao Liu, Yajuan Han, Hongya Chen, Shaobo Qu
Opto-Electronic Advances   2023 **6**, 220148   doi: 10.29026/oea.2023.220148

All-optical logic gate computing for high-speed parallel information processing
Shuming Jiao, Junwei Liu, Liwen Zhang, Feihong Yu, Guomeng Zuo, Jingming Zhang, Fang Zhao, Weihao Lin, Liyang Shao
Opto-Electronic Science   2022 **1**, 220010   doi: 10.29026/oes.2022.220010

Benchmarking deep learning-based models on nanophotonic inverse design problems
Taigao Ma, Mustafa Tobah, Haozhu Wang, L. Jay Guo
Opto-Electronic Science   2022 **1**, 210012   doi: 10.29026/oes.2022.210012

More related article in Opto-Electron Journals Group website ⎘

Pattern recognition in multi-synaptic photonic spiking neural networks based on a DFB-SA chip

Yanan Han[1], Shuiying Xiang[1]*, Ziwei Song[1], Shuang Gao[1], Xingxing Guo[1], Yahui Zhang[1], Yuechun Shi[2], Xiangfei Chen[3] and Yue Hao[1]

Spiking neural networks (SNNs) utilize brain-like spatiotemporal spike encoding for simulating brain functions. Photonic SNN offers an ultrahigh speed and power efficiency platform for implementing high-performance neuromorphic computing. Here, we proposed a multi-synaptic photonic SNN, combining the modified remote supervised learning with delay-weight co-training to achieve pattern classification. The impact of multi-synaptic connections and the robustness of the network were investigated through numerical simulations. In addition, the collaborative computing of algorithm and hardware was demonstrated based on a fabricated integrated distributed feedback laser with a saturable absorber (DFB-SA), where 10 different noisy digital patterns were successfully classified. A functional photonic SNN that far exceeds the scale limit of hardware integration was achieved based on time-division multiplexing, demonstrating the capability of hardware-algorithm co-computation.

Keywords: photonic spiking neural network; fabricated DFB-SA laser chip; multi-synaptic connection; optical computing

Introduction

By drawing on the structure and information processing of the nervous system, the new paradigm of neuromorphic computing with non-von Neumann architectures has driven further development of low-power and low-latency computing systems. Nowadays, neuromorphic learning is mostly software-based and inherently limited by the von Neumann bottleneck. Spiking neural networks (SNNs), known as the third-generation neural networks, are considered to be the most bio-realistic[1,2]. SNNs employ spatiotemporal coding, and exploit low-power characteristics due to sparse spike transmission[3–6]. The SNN architecture mainly consists of three parts, the neural computational units, synaptic connections, and learning rules.

As the most important element in neural networks, theoretical models and hardware emulations of neurons have received extensive attention in both the electrical and optical domains. However, due to the complex biological mechanisms of neurons, the cells and synapses of neurons are usually treated separately as nonlinear computational units and tunable connections in artificial

[1]State Key Laboratory of Integrated Service Networks, State Key Discipline Laboratory of Wide Bandgap Semiconductor Technology, Xidian University, Xi'an 710071, China; [2]Yongjiang Laboratory, Ningbo 315202, China; [3]Key Laboratory of Intelligent Optical Sensing and Manipulation, Ministry of Education, the National Laboratory of Solid State Microstructures, the College of Engineering and Applied Sciences, Institute of Optical Communication Engineering, Nanjing University, Nanjing 210023, China.

*Correspondence: SY Xiang, E-mail:syxiang@xidian.edu.cn

neural networks.

In the field of microelectronics, neurons based on complementary metal-oxide-semiconductor technology memristor arrays[7–10], transistors[11,12] and VLSIs[13] have achieved tremendous improvements. While such microelectronic neurons can exceed biological time scales, they are subject to fundamental bandwidth fan-in trade-offs and suffer from deficiencies in energy efficiency, speed, etc.[14]. Due to the high speed, high bandwidth, and achievable low crosstalk of optical platforms, optical computing has attracted lots of attention[15–21], including linear computing such as matrix multiplication[15,16], all optical logic gate[17], photonic synapses and neurons[21], etc. Photonic neurons have received increasing attention as a promising candidate for artificial neurons, and a great deal of effort has been devoted to the exploration of photonic devices.

To date, significant efforts have been dedicated to emulating photonic spiking neurons. The basic neuron-like dynamics such as spiking, integration, threshold behavior and relative refractory period have been observed in various types of lasers[22], including ring lasers[23], vertical cavity surface emitting semiconductor lasers (with a saturable absorber)[24–27], distributed feedback semiconductor (DFB) lasers, and DFB lasers with a saturable absorber (DFB-SA)[28–30], Fabry-Pérot lasers with a saturable absorber (FP-SA)[31], semiconductor micropillar lasers[32], etc. Based on the nonlinear computing of photonic spiking neurons, photonic SNNs have been implemented for simple pattern recognition[31,33] and sound direction detection[28] with the help of algorithms. In photonic SNNs, the basic feed-forward structure is the most adopted. However, in biological nervous systems, the neural coupling is usually not unidirectional and unique. There may be multiple coupling paths between two neurons with different efficacies and delays[34–37]. However, there is not much attention paid on the impact of multiple connections in optical computing.

Here, we present a supervised learning scheme in temporal encoding photonic SNN for pattern classification with the introduction of multisynapse couplings and provide experimental demonstration via a fabricated DFB-SA chip. The main contributions of this work lie in: Firstly, we introduce multisynapse couplings in photonic SNN for the first time, where multiple coupling paths between two neurons with different efficacies and delays are considered. Then, the digit pattern classification is performed numerically to demonstrate the improvements of network performance. Finally, the collaborative learning of algorithms and hardware devices is further demonstrated experimentally based on a single fabricated DFB-SA chip via using time-multiplexed spike encoding.

Methods

Experimental setup

The multi-synaptic connection in the biological neural network is illustrated in Fig. 1(a), where synaptic connections from presynaptic neurons are distributed in the dendritic tree of the postsynaptic neuron[36]. The soma in the postsynaptic neuron integrates the received signals and converts the input signals into spike forms. The coupling delay and efficacy of synapses differ.

In the experiment, we adopted a fabricated DFB-SA chip to perform the nonlinear activations of the postsynaptic neuron. The experimental setup used for verifying the nonlinear computing based on the DFB-SA spiking neuron is presented in Fig. 1(b). The GDS profile and chip micrograph of the DFB-SA are illustrated respectively. The system mainly consists of the core computing chip and the peripheral circuit for modulation and control. In the experiment, the gain region of the DFB-SA is driven by a current source, denoted as the gain current I_G, while the SA region is reversely driven by a voltage source, denoted as V_{SA}. A tunable laser (TL; AQ2200-136 TLS module, Yokogawa) is used to provide the optical carrier with a center wavelength of λ_{inj}. The input spike sequence is firstly written into the arbitrary waveform generator (AWG; AWG70001A, Tektronix) with a sampling rate of 10.5 GHz, then modulated into the optical carrier through a Mach-Zehnder modulator (MZM, Fujitsu FTM7928FB). After power control with a variable optical attenuator (VOA), the modulated signal is injected into the DFB-SA via a three-port optical circulator (CIRC). The modulated optical signal and the output of the DFB-SA are converted to electrical signals by photodetectors (PDs, Agilent HP11982A), recorded and observed by an oscilloscope (OSC, Keysight DSOV334A). The optical spectrum of the DFB-SA is recorded and analyzed by an optical spectrum analyzer (OSA, Advantest Q8384).

The two-section structure of DFB-SA allows it to simulate the basic dynamics of leaky-integrate and fire (LIF) neurons. We firstly demonstrate the integrattion and threshold behaviors of the photonic spiking neuron. Dif-
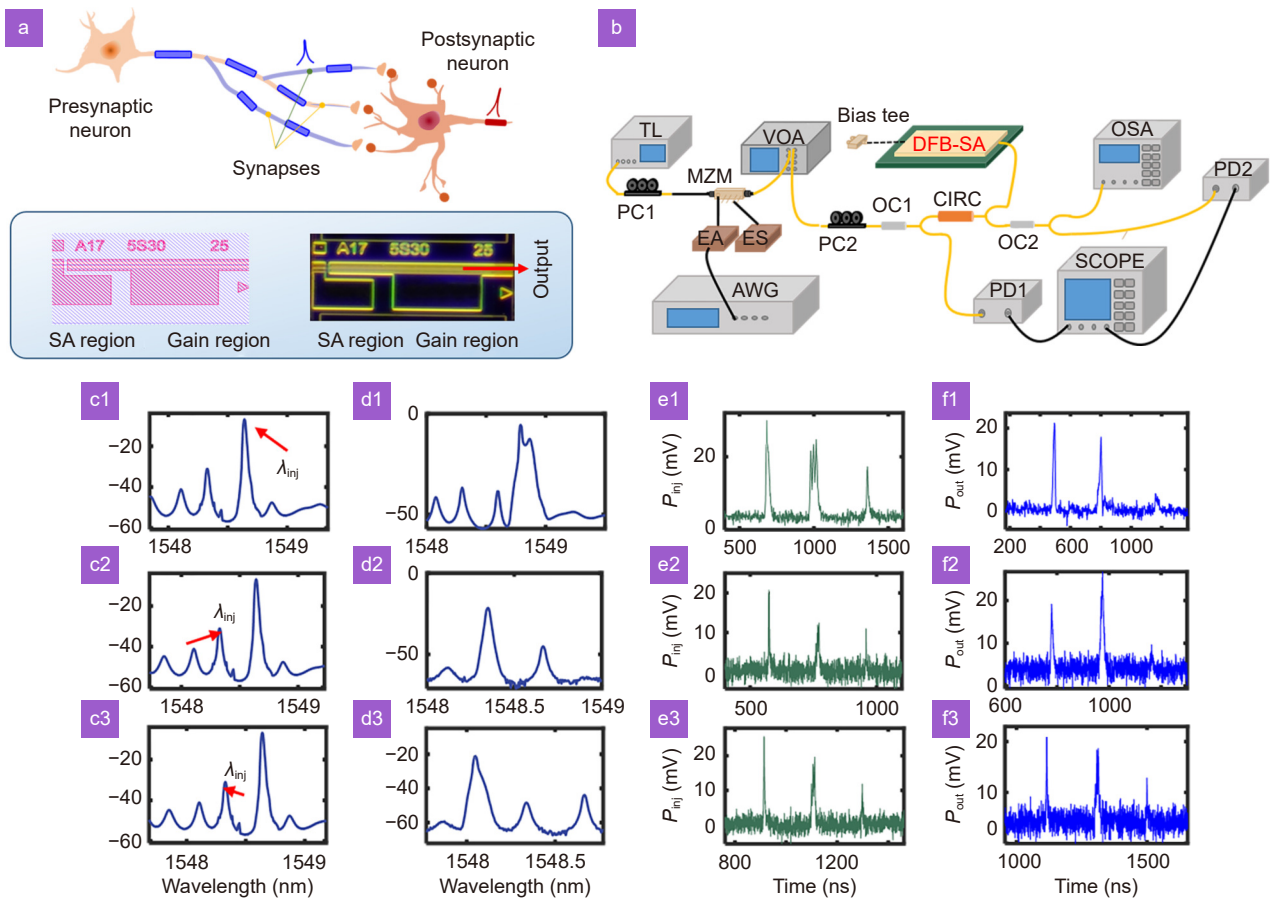
Fig. 1 | (**a**) The geometry of multi-synaptic connections. (**b**) The experimental setup. The optical path is denoted by yellow, and the electrical path is black. The GDS file and chip micrograph of the DFB-SA neuron chip. (**c1–c3**) The optical spectrum of free-running DFB-SA, marked with different injection wavelengths. (**d1–d3**) The optical spectrum of DFB-SA with external optical injection corresponding to (c1–c3). (**e1–e3**) and (**f1–f3**) The input pattern and the corresponding output.

ferent injection methods are compared. We consider coherent injection when the injection wavelength λ_{inj} is close to the dominate mode, and incoherent injection when λ_{inj} is away from the dominant mode. Figure 1(c1–c3) show the optical spectrum of free-running DFB-SA. The external optical signal is injected into the dominate mode (λ_{inj}=1548.64 nm), the first side mode (λ_{inj}=1548.33 nm) and the second side mode (λ_{inj}= 1548.11 nm), respectively. The corresponding optical spectrum with external optical injection is presented in Fig. 1(d1–d3). The input pattern is encoded into several spikes with different amplitude and distance (Fig. 1(e1–e3)). The first high spike is used to demonstrate the spiking dynamics of DFB-SA. The second weak spike is actually a cluster of several very close spikes, for the revealing of integration behavior. The third single weak spike is used for threshold demonstration. The corresponding output pattern is shown in Fig. 1(f1–f3). We can observe that when injected into the dominate mode and

the first side mode, the single weak pulse causes no obvious spike generation, however a cluster of spikes with similar amplitude can make the neuron generate a clear spike that is similar to the spike generated via a single high pulse, demonstrating the integration and threshold dynamics of the photonic spiking neurons. However, when injected into the second side mode which is more far from the dominate mode, the neuron responds almost consistent with the input. Hence, we adopt coherent injection to perform pattern classification in the following.

Algorithms comparison

To accomplish efficient hardware-based computation, the basic architecture for temporal-coding supervised learning in SNN is introduced here, which consists of 5 parts, including the spatio-temporal encoding part, the input layer, the reconfigurable weight and delay arrays, the output layer, and the control unit. As shown in Fig. 2,
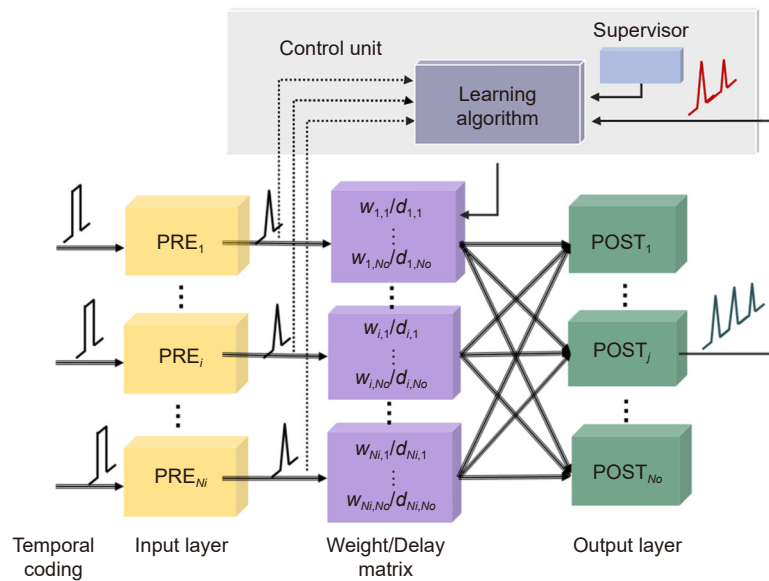
Fig. 2 | The basic structure for supervised learning of photonic SNNs with temporal coding.

in the encoding part, all input features are encoded into rectangular pulses, with the central timing carrying the specific feature. The pulse width and strength are properly selected to stimulate a single spike in the photonic spiking neuron of the input layer. The optical spikes generated from the input layer are then transmitted into the output layer, delayed and weighted separately via the delay and the weight arrays. The feedforward signals are received and activated via the output neuron. If the received inputs raise the carrier density of the output laser neuron above the threshold, which is also determined by the bias current of the gain region, a spike is generated, otherwise, the output neuron remains silent.

The output spike timing and the input spike timing are detected in the control unit. In accordance with the algorithm, the weight and delay arrays are adjusted based on the calculated updates. In photonic SNNs, typically only online inference is conducted due to the challenges associated with controlling and storing optical signals. Once the weights and time delays are trained, they are configured into the network, enabling high-speed inference calculations at the velocity of light.

Here, we employed multi-synaptic connections in photonic SNNs to achieve 0~9 digit pattern classification. The processing is shown in Fig. 3(a). Each digit consists of a 20×20 pixel matrix, resulting in a 400-dimensional feature vector. Due to the relative simplicity of the task, the 400-dimensional input vectors were first reduced to 9 dimensions using principal component analysis in order to reduce the computational effort. Subsequently, the reduced input vector was transformed in-

to rectangular spikes with distinct central timings based on the corresponding feature values, as illustrated in Fig. 2. After temporal encoding, the features were fed into the SNN. Each input neuron was connected to an output neuron through multiple synapses N_{syn}, each possessing a different weight and time delay. Because there were multiple output neurons, the outputs of the neurons were encoded according to a set of orthogonal unit vectors, akin to the one-hot label. The dimension of the vector corresponds to the number of categories that need to be classified. For a neural network with input dimension N_i and output dimension N_o, when the k-th class sample ($k=1,…,K$; $K=N_o$) is fed in, the target vector is defined as $t_{dk} \cdot e_k$, where e_k denotes the k-th set of unit vectors. Consequently, the input of the k-th class samples is expected to elicit an active response from the k-th output neuron, while the other output neurons remain inactive, as illustrated in Fig. 3(b). In this task, the network size is determined by the input feature dimension and categories, namely, $N_i = 9$, $N_o = 10$.

Predictably, multi-synaptic coupling enables robust information afference in a network. In the case that some pathways are disrupted, information can still be delivered via alternative ways. In addition, different coupling efficiencies and delays introduce noise in the network, which can prevent overfitting and to some extent improve the performance of the system.

In the following, to verify the role of multi-synaptic structures in pattern recognition tasks, we compare several common algorithms for temporal-coding feed-forward SNN training, including the well-known remote
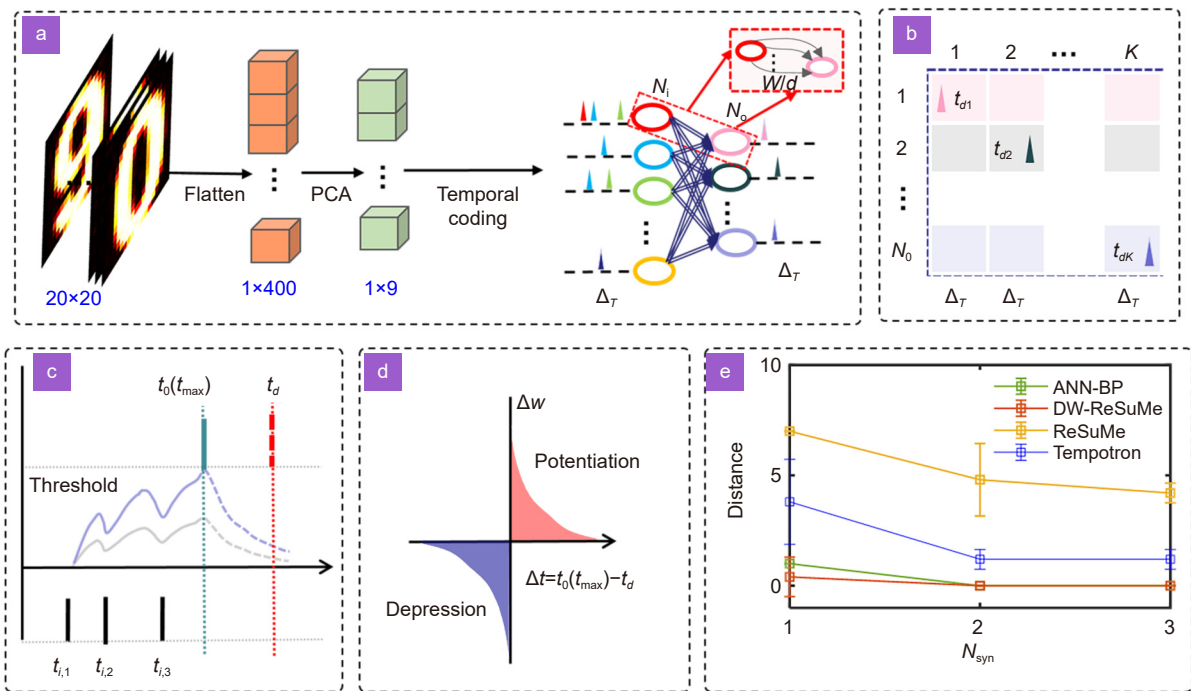
Fig. 3 | (a) The process of digit pattern recognition based on a multi-synaptic photonic spiking neural network. **(b)** The output classification. **(c)** The basic principle for temporal coding SNN. **(d)** The STDP rule. **(e)** The mean distance of 4 different training methods with different N_{syn}.

supervised method (ReSuMe)[38,39], Tempotron[31,40], and delay-weight combined ReSuMe (DW-ReSuMe)[41–43]. The principle for training a temporal coding SNN is displayed in Fig. 1(c). The weight is updated based on the difference of input spiking timing t_i, the output spiking timing t_o, or the peak timing $t_{\max}$ if no spike is generated according to different algorithms. The optical spiking timing-dependent plasticity (STDP)[39,43] is combined to replace the kernel function. The traditional back-propagation method is also considered to provide a baseline.

To quantitatively describe the degree of convergence of the training process, we define Distance as the average of the differences between the targets assigned to all the output neurons and their actual behaviors for all input samples:

$$Distance = \frac{1}{K}\frac{1}{N_{\mathrm{o}}}\sum_{k=1}^{K}\sum_{j=1}^{N_{\mathrm{o}}}d_{kj}$$

$$\begin{cases} d_{kj} = 0 \text{ if } (n_d^{kj}=0, n_0^{kj}=0, \text{ or } n_d^{kj}=1,\, n_{\mathrm{o}}\neq 0) \\ d_{kj} = 1 \text{ otherwise} \end{cases},\quad (1)$$

where $k=1,\ldots,K$ denotes the index of pattern categories, and $j=1,\ldots,N_{\mathrm{o}}$ is the index of output neurons. d_{kj} describes the distance between the target assigned to the j-th output neuron when the k-th category is input, n_d^{kj} is the corresponding target spike number which is 0 when the neuron is expected to be silent, and n_o^{kj} is the actual

output spike number. The average distance will be 0 when all the output neurons emit spikes according to their targets. For the BP method, the Distance can be calculated equivalently as the number of misclassified samples.

During the training process, the parameters of each synapse are adjusted independently according to the algorithm. Note the difference in the dimension of output neurons, when the target neuron is expected to generate a spike, the other neurons need to be silent. The results are given in Fig. 3(e). From where we can observe that with increasing N_{syn}, the Distance of the network tends to be lower. When $N_{\mathrm{syn}}=1$, only the Distance calculated with DW-ReSuMe could converge to 0, indicating the highest calculation efficiency for simple pattern learning. We also test these methods based on a much more complex dataset MNIST. For each categories of hand-written digits, we randomly chose 20 samples from the training set and 10 samples from the test set. The selected dataset is further down-sampled via PCA to decrease the input dimension from 784 to 20. Moreover, to provide a baseline performance of the selected dataset, the convolutional neural network (CNN) and traditional artificial neural network (ANN) are also considered. 16 kernels with size 2×2 are used, so the input size of the fully connection layer is 28×28×16. The results are given in Table 1. It can be seen that in CNN with a single convolution

Table 1 | Accuracy of MNIST classification based on different models with different N_{syn}.

Algorithm	Network size	N_{syn}=1	N_{syn}=2	N_{syn}=3
Tempotron	20×10	(25.71±2.43)%	(30.4±3.51)%	(34.80±2.68)%
ReSuMe	20×10	(19.4±2.19)%	(27.75±5.56)%	(29.60±4.10)%
DL-ReSuMe	20×10	(37±7.78)%	(42.80±1.30)%	(47.20±2.39)%
ANN-BP	20×10	(54.60±7.13)%	(56.67±5.28)%	(60.67±3.14)%
CNN-BP	(784×16)×10	(79.4±1.52)%		/

and pooling layer, the mean accuracy could reach 80%. Then, the down sampled features are trained with 4 algorithms in the same network structure, and different numbers of synapses are compared. Not surprisingly, the ANN provide the best performance when N_{syn}=3, reaching 60.67%. As for the temporal coding SNN algorithm, the DW-ReSuMe still performs better than ReSuMe and Tempotron. Overall, with multiple synapses, the mean accuracy increases for all methods.

Experimental validation

Feasibility analysis

In the previous section, it is demonstrated that in temporal coding SNN, the DW-ReSuMe performs well in comparison with other well-known methods. In this part, the DW-ReSuMe is adopted for further analysis. The classification of 0~9 digit patterns shown in Fig. 4 is performed based on the proposed network structure in

conjunction with the modified DW-ReSuMe algorithm. Here, triple-synaptic connections are considered. The target timing for all 10 patterns is set to t_d=23 ns, whereas for neurons not expected to generate spikes, the corresponding target is set to the maximum simulation time T, where T = 40 ns. Figure 4 further illustrates the training process for all 10 output neurons when exposed to different input patterns. The rows in the figure indicate different output neurons and the columns correspond to different input patterns. It is evident that after several training epochs, all the output neurons produce a single spike at around 23 ns only when the corresponding category is input, while the other neurons remain resting.

Then, we trained the neural network with varying numbers of synaptic connections to investigate the effect of multi-synapses on the network performance. The results are presented in Fig. 5(a). As can be seen, when there is only one synapse, the training process is not stable,
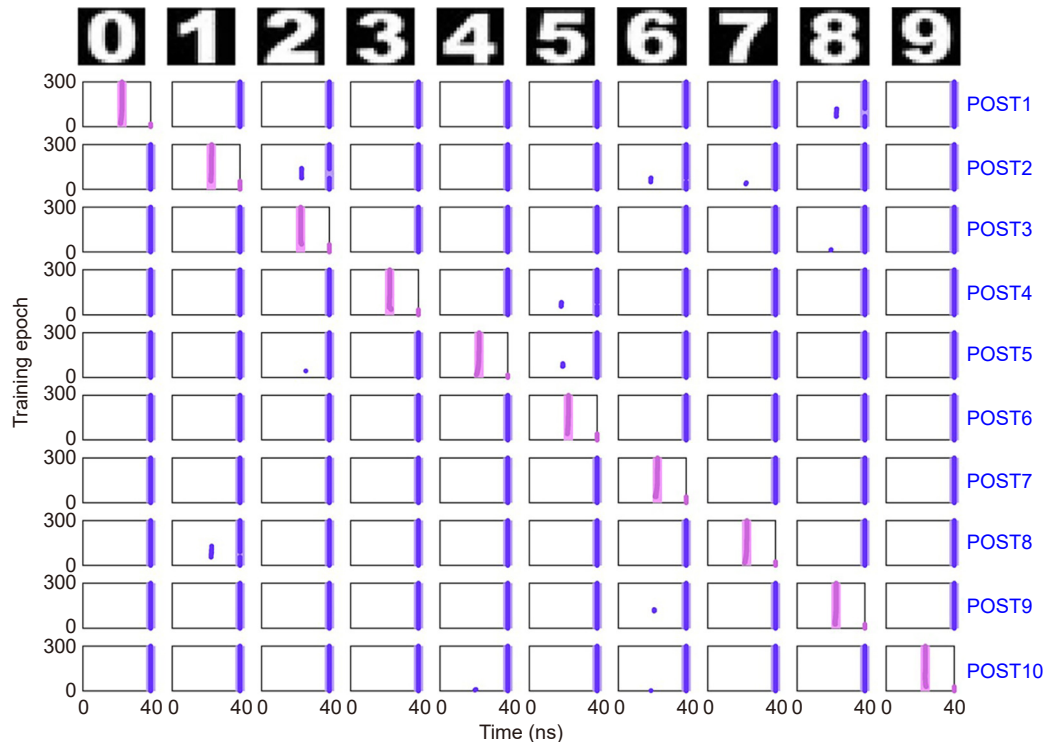

Fig. 4 | The output spike timing of all 10 output neurons (the row) at the input of all 10 patterns (the column) when N_{syn}=3.
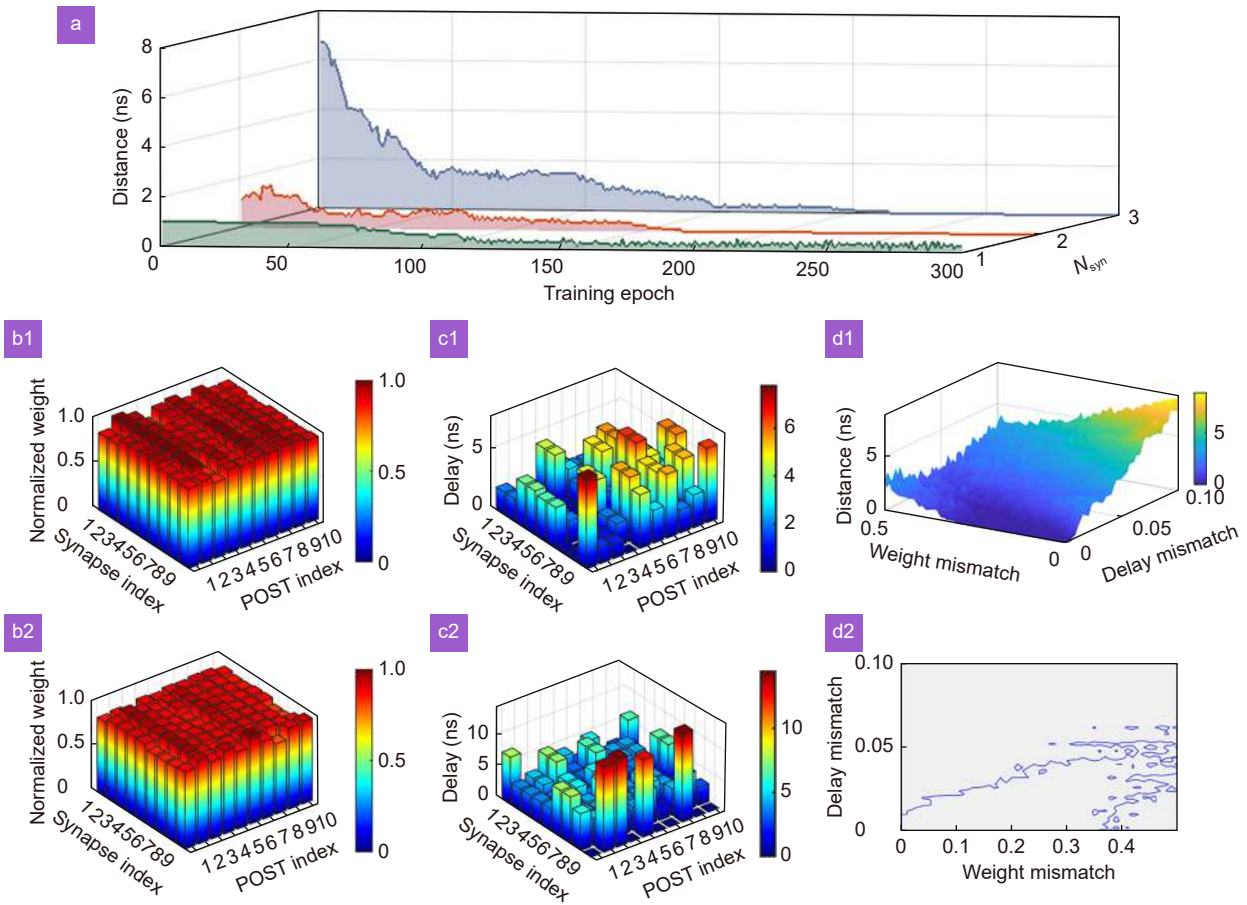
Fig. 5 | (a) The converged Distance with 1, 2, and 3 synapses, respectively. **(b1–b2)** Normalized weights for each of the two sets of synapses after convergence. **(c1–c2)** Normalized delays for each of the two sets of synapses after convergence. **(d1)** The converged Distance in the parameter space of weight mismatch and delay mismatch and **(d2)** projection of the contour with *Distance*=1.

and the error distance fails to converge to 0. However, when two synapses are present, the distance converges to 0 after approximately 168 training cycles. Similarly, with three synapses, the error distance converges at the 214th training cycle. It is worth noting that the presence of three synapses introduces more learning parameters, making the network training more complex and resulting in a larger initial error. Therefore, it is not necessary to use as many synapses as possible to enhance network performance. Instead, a trade-off should be made between performance and training efficiency.

For this task, the network performs best when N_{syn}=2. In the following, we consider the case when N_{syn}=2 for further analysis. Figure 5(b1–b2) and 5(c1–c2) present the weights and delays of the two sets of synapses after training convergence, noting that the initial values of weight and time delay for all synapses are uniform. It can be observed that the weights of the two groups of synapses change slightly compared to the change in delays, indicating that delay is a critical parameter in the tem-

poral coding learning method. Besides, as the parameters of the two groups of synapses were trained independently, the final results also differed significantly.

Furthermore, we conducted an analysis to assess the robustness of the network by investigating the impact of deviations in weight and delay configurations on its performance. To quantitatively characterize the introduced parameter mismatches, the weights were normalized to 1 and the time delays were normalized to 1 ns. Gaussian noise with intensities ranging from 0 to 0.5 for weights and from 0 to 0.1 ns for time delays was then added. The calculation was repeated five times to obtain an average result, as depicted in Fig. 5(d1). The solid blue line in Fig. 5(d2) represents a contour projection with a Distance value of 1. Within the contour, the average distance is below 1, indicating the range of convergence. Notably, the network demonstrates low sensitivity to weight mismatches, but exhibits considerable sensitivity to deviations in time delays. A relative mismatch degree greater than 0.01 in time delays can lead to a significant decline

in performance.

Experimental results and discussion

In the collaborative implementation of algorithms and hardware, input patterns with a delay noise of 0.01 and weight noise of 0 are selected. As can be seen from Fig. 5(d2), this condition corresponds to the boundary of convergence. Notice that the multi-synaptic network is essentially equivalent to feeding the same feature through multiple monosynaptic input neurons. After training convergence, for each sample, the input feature is first delayed and weighted via the trained weights and delays, then summated to form a single spike train, which represents exactly the input signals received by the single postsynaptic neuron. The spike sequence written into AWG is the delayed and weighted sum of all en-

coded features. Based on the DFB-SA chip, the outputs of all POST neurons are observed simultaneously using the time-division multiplexing method, as illustrated in detail in Fig. 6.

Figure 6(a1–j1) present the input encoding sequences for all the 10 input patterns, with each cycle containing 10 spike clusters representing the cumulative input signal received by each of the 10 output neurons. Each cluster comprises 18 spikes of varying intensities, representing the input signals afferent from the 9 input neurons each with 2 synapses. The corresponding output sequences from DFB-SA are shown in Fig. 6(a2–j2). Two cycles of the output patterns are shown in each subplot. For each input pattern, a spike can be elicited in the corresponding output neuron, while the rest of the neurons produce only low-amplitude perturbations, which are
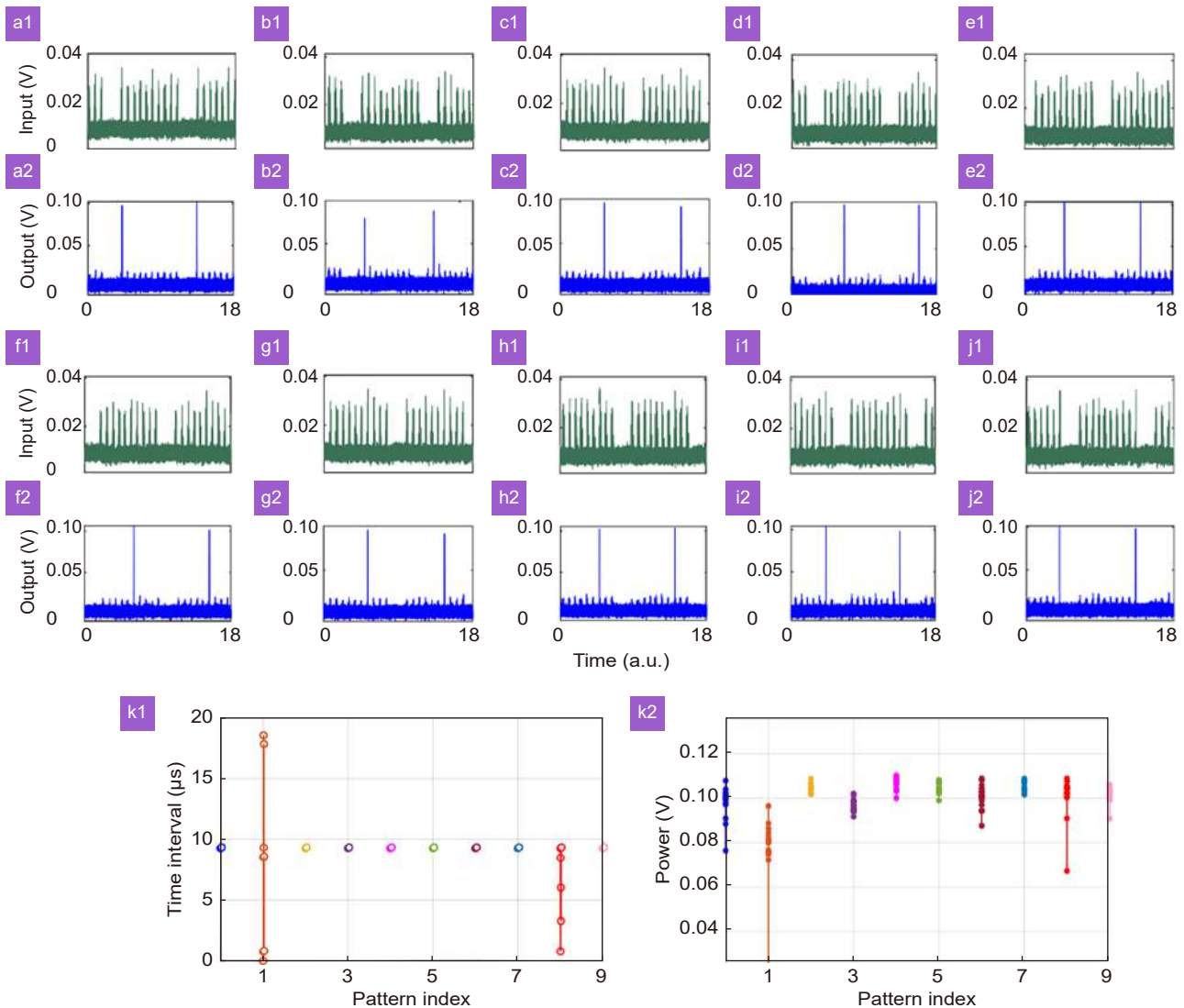

Fig. 6 | (a1–j1) The input spike patterns for all the 10 output neurons. **(a2–j2)** The correlated outputs of DFB-SA. **(k1)** The output spike interval for all 10 output neurons of 20 experiment trials. **(k2)** The output spike power for all 10 output neurons of 20 experiment trials.

consistent with the simulation results.

To analyze the stability of the experimental results, we repeated each set of experiments 20 times and recorded the timing and amplitude of the output spikes. Figure 6(k1) illustrates the spike time interval of the output spike train across 20 experiments for all 10 patterns. We can see that in most cases, the spike interval is quite stable, demonstrating the stability of the photonic spiking neuron. However, for pattern 1 and pattern 8, the output spike is not stable because of the introduced noise as discussed earlier. It should be noted that working within the convergence region of parameter mismatches yields more stable results. Likewise, the spike amplitudes of the output spike trains across the 20 experiments for all 10 patterns are depicted in Fig. 6(k2). It can be observed that, compared to the spike timing intervals, the spike amplitudes display greater fluctuations. The amplitude fluctuation poses a problem of threshold selection to determine whether a spike is generated, which is less crucial in the inference of photonic SNN with temporal coding since information is carried in the specific timing of spikes.

Finally, the power consumption of the DFB-SA laser neuron is estimated. All the peripheral circuits are neglected, and we only focus on the power consumed by the DFB-SA for nonlinear computing. The power consumption can be calculated as the power difference of the modulated signals P_{inj1} =31.09 μW (which is able to trigger a single spike) and the power before modulation P_{inj2} =30.53 μW. That is to say, the power consumption of the nonlinear computing in DFB-SA is about 0.36 μW, which is comparable with the result obtained by an FP-SA[31].

Conclusions

In this work, we proposed the use of multi-synaptic connectivity in photonic SNN with the modified ReSuMe algorithms based on delayed-weight co-training. We identified 0~9 digit patterns through numerical simulations and experiments. By investigating the effect of different numbers of synaptic couplings between input and output neurons, we found that multiple connections could effectively improve network performance. We also analyzed the robustness of the network by assessing the convergence of the network for different degrees of configuration errors in weights and delays. Finally, the collaborative computing of algorithm and hardware was implemented based on a single DFB-SA chip using a time-

multiplexing approach. This work demonstrates efficient learning in photonic SNN via introducing multiple synapses, which is helpful in the future application of optical computing.

References

1. Moradi S, Qiao N, Stefanini F, Indiveri G. A scalable multicore architecture with heterogeneous memory structures for dynamic neuromorphic asynchronous processors (DYNAPs). *IEEE Trans Biomed Circuits Syst* **12**, 106–122 (2018).

2. Rathi N, Chakraborty I, Kosta A, Sengupta A, Ankit A et al. Exploring neuromorphic computing based on spiking neural networks: algorithms to hardware. *ACM Comput Surv* **55**, 243 (2023).

3. Roy K, Jaiswal A, Panda P. Towards spike-based machine intelligence with neuromorphic computing. *Nature* **575**, 607–617 (2019).

4. Ponulak F, Kasinski A. Introduction to spiking neural networks: information processing, learning and applications. *Acta Neurobiol Exp* **71**, 409–433 (2011).

5. Taherkhani A, Belatreche A, Li YH, Cosma G, Maguire LP et al. A review of learning in biologically plausible spiking neural networks. *Neural Netw* **122**, 253–272 (2020).

6. Nandakumar SR, Boybat I, Le Gallo M, Eleftheriou E, Sebastian A et al. Experimental demonstration of supervised learning in spiking neural networks with phase-change memory synapses. *Sci Rep* **10**, 8080 (2020).

7. Sengupta A, Banerjee A, Roy K. Hybrid spintronic-CMOS spiking neural network with on-chip learning: devices, circuits, and systems. *Phys Rev Appl* **6**, 064003 (2016).

8. Sengupta A, Panda P, Wijesinghe P, Kim Y, Roy K. Magnetic tunnel junction mimics stochastic cortical spiking neurons. *Sci Rep* **6**, 30039 (2016).

9. Jo SH, Chang T, Ebong I, Bhadviya BB, Mazumder P et al. Nanoscale memristor device as synapse in neuromorphic systems. *Nano Lett* **10**, 1297–1301 (2010).

10. Boybat I, Le Gallo M, Nandakumar SR, Moraitis T, Parnell T et al. Neuromorphic computing with multi-memristive synapses. *Nat Commun* **9**, 2514 (2018).

11. Cassidy AS, Merolla P, Arthur JV, Esser SK, Jackson B et al. Cognitive computing building block: a versatile and efficient digital neuron model for neurosynaptic cores. In *Proceedings of 2013 International Joint Conference on Neural Networks* 1–10 (IEEE, 2013); http://doi.org/10.1109/IJCNN.2013.6707077.

12. Kim H, Hwang S, Park J, Yun S, Lee JH et al. Spiking neural network using synaptic transistors and neuron circuits for pattern recognition with noisy images. *IEEE Electron Device Lett* **39**, 630–633 (2018).

13. Erdener Ö, Ozoguz S. A new neuron and synapse model suitable for low power VLSI implementation. *Analog Integr Circ Sig Process* **89**, 749–770 (2016).

14. Schuman CD, Potok TE, Patton RM, Birdwell JD, Dean ME et al. A survey of neuromorphic computing and neural networks in hardware. arXiv: 1705.06963, 2017. https://doi.org/10.48550/arXiv.1705.06963

15. Meng XY, Zhang GJ, Shi NN, Li GY, Azaña J et al. Compact optical convolution processing unit based on multimode interference. *Nat Commun* **14**, 3000 (2023).

16. Ohno S, Tang R, Toprasertpong K, Takagi S, Takenaka M. Si microring resonator crossbar array for on-chip inference and training of the optical neural network. *ACS Photonics* **9**, 2614–2622 (2022).

17. Jiao SM, Liu JW, Zhang LW, Yu FH, Zuo GM et al. All-optical logic gate computing for high-speed parallel information processing. *Opto-Electron Sci* **1**, 220010 (2022).

18. Huang CR, Sorger VJ, Miscuglio M, Al-Qadasi M, Mukherjee A et al. Prospects and applications of photonic neural networks. *Adv Phys:X* **7**, 1981155 (2022).

19. Gu JQ, Feng CH, Zhu HQ, Chen RT, Pan DZ. Light in AI: toward efficient neurocomputing with optical neural networks—a tutorial. *IEEE Trans Circuits Syst II:Express Briefs* **69**, 2581–2585 (2022).

20. Zhao AK, Jiang N, Peng JF, Liu SQ, Zhang YQ et al. Parallel generation of low-correlation wideband complex chaotic signals using CW laser and external-cavity laser with self-phase-modulated injection. *Opto-Electron Adv* **5**, 200026 (2022).

21. Li CH, Du W, Huang YX, Zou JH, Luo LZ et al. Photonic synapses with ultralow energy consumption for artificial visual perception and brain storage. *Opto-Electron Adv* **5**, 210069 (2022).

22. Xiang SY, Han YN, Song ZW, Guo XX, Zhang YH et al. A review: photonics devices, architectures, and algorithms for optical neural computing. *J Semicond* **42**, 023105 (2021).

23. Coomans W, Gelens L, Beri S, Danckaert J, Van der Sande G. Solitary and coupled semiconductor ring lasers as optical spiking neurons. *Phys Rev E* **84**, 036209 (2011).

24. Scirè A, Mulet J, Mirasso CR, Miguel MS. Intensity and polarization self-pulsations in vertical-cavity surface-emitting lasers. *Opt Lett* **27**, 391–393 (2002).

25. Xiang SY, Zhang H, Guo XX, Li JF, Wen AJ et al. Cascadable neuron-like spiking dynamics in coupled VCSELs subject to orthogonally polarized optical pulse injection. *IEEE J Sel Top Quantum Electron* **23**, 1700207 (2017).

26. Robertson J, Hejda M, Zhang YH, Bueno J, Xiang SY et al. Neuromorphic object edge detection with artifical photonic spiking VCSEL-neurons. In *Proceedings of 2020 IEEE Photonics Conference* 1–2 (IEEE, 2020); http://doi.org/10.1109/IPC47351.2020.9252334.

27. Chen ZJ, Sludds A, Davis R, Christen I, Ateshian L et al. Coherent VCSEL network computing. In Proceedings of the 27th OptoElectronics and Communications Conference (OECC) and 2022 International Conference on Photonics in Switching and Computing (PSC) 1–3 (IEEE, 2022); http://doi.org/10.23919/OECC/PSC53152.2022.9849860.

28. Ma BW, Zou WW. Demonstration of a distributed feedback laser diode working as a graded-potential-signaling photonic neuron and its application to neuromorphic information processing. *Sci. China Inf. Sci* **63**, 160408 (2020).

29. Shi YC, Xiang SY, Guo XX, Zhang YH, Wang HJ et al. Photonic integrated spiking neuron chip based on a self-pulsating DFB laser with a saturable absorber. *Photonics Res* **11**, 1382–1389 (2023).

30. Xiang SY, Shi YC, Zhang YH, Guo XX, Zheng L et al. Photonic integrated neuro-synaptic core for convolutional spiking neural network. arXiv: 2306.02724, 2023. https://doi.org/10.48550/arXiv.2306.02724

31. Xiang SY, Shi YC, Guo XX, Zhang YH, Wang HJ. et al. Hardware-algorithm collaborative computing with photonic spiking neuron chip based on an integrated Fabry–Perot laser with a saturable absorber. *Optica* **10**, 162–171 (2023).

32. Selmi F, Braive R, Beaudoin G, Sagnes I, Kuszelewicz R et al. Relative refractory period in an excitable semiconductor laser. *Phys Rev Lett* **112**, 183902 (2014).

33. Feldmann J, Youngblood N, Wright CD, Bhaskaran H, Pernice WHP. All-optical spiking neurosynaptic networks with self-learning capabilities. *Nature* **569**, 208–214 (2019).

34. Fauth MJ, Wörgötter F, Tetzlaff C. Collective information storage in multiple synapses enables fast learning and slow forgetting. *BMC Neurosci* **16**, O15 (2015).

35. Federmeier KD, Kleim JA, Greenough WT. Learning-induced multiple synapse formation in rat cerebellar cortex. *Neurosci Lett* **332**, 180–184 (2002).

36. Golding NL, Staff NP, Spruston N. Dendritic spikes as a mechanism for cooperative long-term potentiation. *Nature* **418**, 326–331 (2002).

37. Hiratani N, Fukai T. Redundancy in synaptic connections enables neurons to learn optimally. *Proc Natl Acad Sci USA* **115**, E6871–E6879 (2018).

38. Ponulak F, Kasiński A. Supervised learning in spiking neural networks with ReSuMe: sequence learning, classification, and spike shifting. *Neural Comput* **22**, 467–510 (2010).

39. Xiang SY, Ren ZX, Song ZW, Zhang YH, Guo XX et al. Computing primitive of fully VCSEL-based all-optical spiking neural network for supervised learning and pattern classification. *IEEE Trans Neural Netw Learn Syst* **32**, 2494–2505 (2021).

40. Gütig R, Sompolinsky H. The tempotron: a neuron that learns spike timing-based decisions. *Nat Neurosci* **9**, 420–428 (2006).

41. Taherkhani A, Belatreche A, Li YH, Maguire LP. DL-ReSuMe: a delay learning-based remote supervised method for spiking neurons. *IEEE Trans Neural Netw Learn Syst* **26**, 3137–3149 (2015).

42. Han YN, Xiang SY, Ren ZX, Fu CT, Wen AJ et al. Delay-weight plasticity-based supervised learning in optical spiking neural networks. *Photonics Res* **9**, B119–B127 (2021).

43. Xiang SY, Gong JK, Zhang YH, Guo XX, Han YN et al. Numerical implementation of wavelength-dependent photonic spike timing dependent plasticity based on VCSOA. *IEEE J Quantum Electron* **54**, 8100107 (2018).

Acknowledgements

Author contributions

YN Han: conceptualization, simulations and partial measurements, visualization, writing-original draft preparation;. SY Xiang: methodology, validation, data curation, funding acquisition, revision; ZW Song, S Gao: experiments, measurements, visualization; XX Guo, YH Zhang: investigation, data curation, revision,; YC Shi, XF Chen: manufacturing, supervision; Y Hao: supervision.

Competing interests